Transarterial Drug Delivery for Liver Cancer: Numerical Simulations and Experimental Validation of Particle Distribution in Patient-Specific Livers

Tim Bomberna, Ghazal Adeli Koudehi, Charlotte Claerebout, Chris Verslype, Geert Maleux & Charlotte Debbaut

In: Expert Opinion on Drug Delivery, published online (2020).

Link: https://doi.org/10.1080/17425247.2021.1853702

Transarterial Drug Delivery for Liver Cancer: Numerical Simulations and Experimental Validation of Particle Distribution in Patient-Specific Livers

Authors: Tim Bomberna [1,2], Ghazal Adeli Koudehi [1], Charlotte Claerebout [1], Chris Verslype [3], Geert Maleux [4,5], Charlotte Debbaut [1,2]

1. IBiTech-bioMMeda, Department of Electronics and Information Systems, Ghent University, Belgium

2. Cancer Research Institute Ghent (CRIG), Ghent University, Belgium

3. Department of Clinical Digestive Oncology, University Hospitals Leuven and KU Leuven, Leuven, Belgium.

4. Department of Radiology, University Hospitals Leuven, Leuven, Belgium

5. Department of Imaging and Pathology, KU Leuven, Belgium

Corresponding author: Tim Bomberna, IBiTech-bioMMeda, Ghent University, Campus Heymans - Blok B, Corneel Heymanslaan 10, 9000 Gent, Belgium. Phone: + 32 (0)9 332 46 21. Email: Tim.Bomberna@UGent.be

Parts of the material contained in this paper were presented at the following meetings: OncoPoint (28/02/2018, Ghent, Belgium), 8th World Congress of Biomechanics (8-12/07/2018, Dublin, Ireland), Modelling and Experiments in Drug Delivery Systems (3-5/09/2018, Glasgow, Scotland), European Society of Artificial Organs Congress (12-15/09/2018, Madrid, Spain), Biomedical Industry Day (13/03/2019, Brussels, Belgium), National Day of Biomedical Engineering (29/11/2019, Brussels, Belgium), Belgian Association for Cancer Research Annual Meeting (07/02/2020, Brussels, Belgium) and Virtual Physiological Human Conference (24-28/08/2020, virtual).

The Version of Record of this manuscript has been published and is available in EXPERT OPINION ON DRUG DELIVERY, 2020,
https://www.tandfonline.com/doi/10.1080/17425247.2021.1853702.

LIST OF ABBREVIATIONS

HCC	Hepatocellular carcinoma
PD	Particle distribution
CFD	Computational fluid dynamics
TACE	Transarterial chemoembolization
TARE	Transarterial radioembolization
PHA	Proper hepatic artery
FD	Flow distribution
HL	Healthy liver
CL	Cirrhotic liver
DPM	Discrete Phase Model
BC	Boundary condition
RL	Right lobe
LL	Left lobe
PRM	Particle Release Map
PEF	Particle exit fraction
PNEF	Particle non-exit fraction
STAR	Spread-to-average ratio
PVC	Polyvinyl chloride

REF	Reservoir exit fraction

ABSTRACT

Background: Transarterial therapies are routinely used for the locoregional treatment of unresectable hepatocellular carcinoma (HCC). However, the impact of clinical parameters (i.e. injection location, particle size, particle density etc.) and patient-specific conditions (i.e. hepatic geometry, cancer burden) on the intrahepatic particle distribution (PD) after transarterial injection of embolizing microparticles is still unclear. Computational fluid dynamics (CFD) may help to better understand this impact.

Methods: Using CFD, both the blood flow and microparticle mass transport were modeled throughout the 3D-reconstructed arterial vasculature of a patient-specific healthy and cirrhotic liver. An experimental feasibility study was performed to simulate the PD in a 3D-printed phantom of the cirrhotic arterial network.

Results: Axial and in-plane injection locations were shown to be effective parameters to steer particles towards tumor tissue in both geometries. Increasing particle size or density made it more difficult for particles to exit the domain. As cancer burden increased, the catheter tip location mattered less. The in vitro study and numerical results confirmed that PD largely mimics flow distribution, but that significant differences are still possible.

Conclusions: Our findings highlight that optimal parameter choice can lead to selective targeting of tumor tissue, but that targeting potential highly depends on patient-specific conditions.

KEY WORDS: biofluid mechanics; computational fluid dynamics; hepatocellular carcinoma; locoregional drug delivery; personalized medicine; transarterial therapy.

ARTICLE HIGHLIGHTS

* Computational fluid dynamics (CFD) is a powerful numerical technique that allows simulating blood and drug particle flow in patient-specific liver vasculatures. CFD can increase our understanding of key factors influencing fluid flow and drug delivery, and can play a role in pre-operative procedure planning.

* The targeting potential – the dependency of particle behavior on controllable injection parameters – varies between the two patients considered in this study, but also varies for different regions within the vasculature of one patient, and for the specific injection parameter considered. This underlines the potency of targeting potential as a relevant metric to evaluate the possible optimization of clinical procedures pre-operatively.

* The focus should be shifted to personalized modelling of particle behavior in patient-specific hepatic arterial geometries, rather than literature-based or simplified patient-inspired geometries.

* Particle destination is clearly correlated with injection location, affirming results from previous studies. However, it should be noted that the possibility to steer particles towards specific outlets depends highly on the possibility to accurately control the catheter tip within the bloodstream, which has not yet proven to be technically feasible up to date.

* In vitro validation showed that flow distribution throughout the hepatic arterial tree is not a perfect surrogate for particle distribution. Hence, it is preferred to model both blood and particle behavior in CFD simulations. Furthermore, the discrepancy between computational and validation results shows that the validation method would benefit from further finetuning.

1. INTRODUCTION

Hepatocellular carcinoma (HCC) is worldwide the most common liver malignancy and a leading cause of cancer-related deaths [1–4]. Due to its high prevalence, HCC has become a global economic burden on society [3]. The WHO estimates that by 2030 more than 1 million people will die of liver cancer yearly [4]. In 80-90% of the patients, HCC develops on a background of liver cirrhosis [4].

HCC patients for whom tumor resection is not possible (e.g. patients with radiologic evidence of vascular invasion, impaired liver function, or non-solitary tumors) can be treated by transarterial therapies such as chemo-embolization (TACE) or radio-embolization (TARE) [3]. During these procedures, the patient is catheterized through the femoral artery and the catheter is retrogradely advanced via the aorta towards the liver. The aim of TACE and TARE is to cut off the blood supply of the tumor tissue by local administration of embolizing microparticles [5]. Since tumor tissue is generally fed by arterial blood, obstruction of these tumor-feeding arteries leads to tumor tissue starvation and death [3]. In TACE, both the embolic and chemotherapeutic effect of the drug-coated particles act complementarily to permanently damage the tumor tissue [6]. In TARE, the embolic effect of the particles is only subsidiary to the local delivery of destructive high-intensity beta-radiation [7]. Since the goal is to limit the particle spread to the surrounding healthy tissue, target specificity is a key parameter of these therapies [8]. Particle injection close to the tumor can increase target specificity. However, vascular access for catheter navigation is often restricted in complicated geometries (such as tortuous blood vessels in cirrhotic and HCC livers [9]), illustrating the need for identifying suitable upstream injection locations. Therefore, this study investigates the feasibility of targeting specific downstream locations starting from easily accessible injection locations in the proper hepatic artery (PHA).

Furthermore, the clinical response to TACE and TARE is highly heterogeneous [10]. It is currently unclear why therapies fail in certain patients and succeed in others. TARE and TACE procedures are also not well standardized [10]. The choice of clinical parameters (e.g. injection location, velocity, dose etc.) and particle properties (e.g. particle size, density etc.), which may impact the particle distribution (PD) [6–9], strongly differs between clinicians and cases, often depending on the preferences and experiences of the clinician. To this end, numerical modeling may play an important role to fully understand, optimize and plan transarterial therapies [15]. As such, this study uses computational fluid dynamics (CFD) to enable studying not only the impact of the parameters mentioned above on the PD, but also the feasibility of therapy optimization by identifying the ideal set of parameters to maximize dose delivery at the tumor site in patient-specific geometries.

Whereas previous numerical CFD studies investigated drug delivery for several applications (e.g. predicting aerosol formation and cellular drug absorption for respiratory drug delivery [16], modelling of aerosol deposition and estimated drug deposition for pulmonary delivery [17]), we focus here on previous studies on transarterial drug delivery in the liver. Kennedy et al. [18] studied particle delivery using steady flow CFD simulations in an idealized literature-based planar hepatic arterial geometry with 5 outlets. Basciano et al. [19] studied the impact of transient flows and particle characteristics in the same simplified geometry, showing that particles could be steered towards the tumor by carefully controlling spatial and temporal injection conditions. While both studies focused on the impact of clinical parameters on the PD to some extent, the interpretation of the results is limited because of the use of a very straightforward, planar geometry. Kleinstreuer et al. [11] investigated the considerable effect of catheter presence on the downstream PD in the same idealized planar geometry and a second, simplified but patient-inspired geometry (assuming perfectly circular blood vessels) with 3 outlets [20]. Again, the interpretation is limited by the simplified geometries. However,

Aramburu et al. [14,21,22] were the first to study particle delivery in a single healthy patient-specific hepatic arterial geometry (although the vessels were reconstructed to be perfectly circular). They developed a method to determine the fractional flow distribution (FD) in such a geometry, considering the liver state (i.e. size and location of the tumor(s)), and concluded that targeting becomes easier in livers with higher cancer burden [12,23]. However, the number of cancer scenarios implemented was limited. Based on their results [11,14,18–20,21,22], Aramburu et al. [24] observed that the liver state, the patient-specific geometry and the axial injection location have a high impact on the PD, while particle properties only have a low impact.

Two other CFD studies assumed the FD to be a surrogate for the PD. While Roncali et al. [25] modelled blood flow in two 3D-reconstructed arterial networks of patient-specific HCC livers, Simoncini et al. [26] similarly modelled two complex geometries but also accounted for smaller vessels (until 0.05 mm) by simulating vascular growth. However, since PD is assumed to be proportional to FD, the modeling approach is insensitive to the impact of injection parameters such as axial or radial injection location or particle properties.

The main limitation of the aforementioned research is that the conclusions are highly geometry-specific and cannot be generalized [24], especially since the study of PD (not only FD) in complex patient-specific livers is very limited with only one healthy geometry [12,14,27]. Moreover, particle delivery in patient-specific diseased livers (such as cirrhosis) was not yet studied, while potentially relevant knowing that cirrhosis severely affects the hepatic (arterial) architecture, which – on its turn –may significantly affect the PD [28]. Other limitations include the overall lack of patient-specific validation of CFD results.

Based on these limitations, this study has a fourfold goal. (i) The impact of specific parameters (particle size, particle density, axial and in-plane injection location) on the PD will be studied in two patient-specific hepatic arterial geometries, being a healthy and a cirrhotic liver. Hereby,

the feasibility of targeting specific vascular zones by injection in the PHA will be estimated. (ii) Furthermore, the impact of vascular complexity (i.e. healthy vs cirrhotic liver) on the PD will be investigated. (iii) Tumor growth will be studied by modeling two cancer situations (tumors in the right or left lobe) at three time points during tumor growth. (iv) The feasibility of testing PD in a patient-specific cirrhotic in vitro phantom will be studied as a proof-of-concept for later studies.

2. MATERIALS & METHODS

2.1. SIMULATION GEOMETRIES AND MESHES

Two patient-specific human liver geometries were used: a healthy liver (HL) and a cirrhotic liver (CL). As was originally approved by the Ethical Committee of the University Hospitals Leuven (Belgium) and by the Belgian Liver and Intestine Committee, these datasets were previously generated by Debbaut et al. [29] and Peeters et al. [9] using a two-step process. First, a vascular corrosion cast of the livers was made resulting in a polymer vascular replica. Secondly, micro-CT scanning resulted in detailed images of the liver casts with a resolution of 110-128 μm [30]. More detailed information on these methodologies can be found in [9,29].

The hepatic arteries were segmented in Mimics software (Materialise, Leuven, Belgium). Only arteries up to the 4th generation were considered for computational purposes. The 3D reconstructions of the arterial trees were further processed (i.e. smoothing, truncating the outlets etc.) in Mimics and 3-matic (Materialise, Leuven, Belgium) resulting in the 3D simulation geometries of Fig. 1.

Subsequently, good quality surface meshes were generated in 3-matic. ICEM CFD (Ansys Inc., Canonsburg, USA) was used to generate volume meshes using the Octree method. The bulk of the volume elements were unstructured tetrahedral elements, complemented by three prism layers at the boundaries to ensure a smooth transition between the walls and the fluid domain.

Mesh densities were increased at the bifurcations to locally capture more complex flow patterns. Mesh sensitivity analyses were performed to determine the most optimal mesh density for the CFD simulations, leading to meshes of $8.9 \cdot 10^6$ and $9.1 \cdot 10^6$ volume elements for the HL and CL, respectively. Minimum and maximum volume of the elements was $3.7 \cdot 10^{-15}$ and $4 \cdot 10^{-12}$ m^3 for the HL and $2.7 \cdot 10^{-16}$ m^3 and $4.9 \cdot 10^{-12}$ m^3 for the CL, respectively.

2.2. NUMERICAL MODEL

The Discrete Phase Model (DPM) in ANSYS Fluent (Ansys Inc., Canonsburg, USA) was used to model the mass transport of the discrete phase (microparticles) dispersed in the continuous phase (blood flow) following a Euler-Lagrangian approach. The DPM was chosen because the particle-fluid mixture can be considered as a dilute suspension.

2.2.1. FLUID PHASE

Blood flow was modeled as laminar flow using the Navier-Stokes equations. The continuity and conservation of momentum equations (1) and (2) were solved in an Eulerian framework.

$$\nabla \cdot \vec{u} = 0 \qquad (1)$$

$$\rho\left(\frac{\partial \vec{u}}{\partial t} + (\vec{u} \cdot \vec{\nabla})\vec{u}\right) = -\nabla p + \nabla \cdot \bar{\boldsymbol{\tau}} + \vec{f} \qquad (2)$$

In Equations (1) and (2), $\vec{u}$ [m/s] is the fluid velocity vector, ρ [kg/m³] is the fluid density for blood, t [s] is time, p [Pa] is the fluid pressure, $\bar{\boldsymbol{\tau}}$ [Pa] is the shear stress tensor and $\vec{f}$ [N/m³] is the force of gravity acting per volume unit on the geometry.

Blood was modelled as an incompressible non-Newtonian fluid using a modified Quemada model for the dynamic viscosity and a density ρ of 1060 kg/m³. This model was proposed by Buchanan et al. [31] and has been used in similar studies for targeted drug delivery

[11,12,14]. As is clear from Equations (3) to (5), the shear stress tensor is a function of the shear rate dependent apparent viscosity, $\mu(\dot{\gamma})$ [Pa· s], which is also a function of hematocrit.

$$\overline{\boldsymbol{\tau}} = \mu(\dot{\gamma})[\nabla\vec{u} + (\nabla\vec{u})^{T}] \quad (3)$$

$$\mu(\dot{\gamma}) = max\{\mu_0, \left(\sqrt{\mu_\infty} + \frac{\sqrt{\tau_0}}{\sqrt{\dot{\lambda}} + \sqrt{\dot{\gamma}}}\right)^2\} \quad (4)$$

$$\dot{\gamma} = \sqrt{\nabla\vec{u}[\nabla\vec{u} + (\nabla\vec{u})^{T}]} \quad (5)$$

In Equations (3) to (5), μ [Pa· s] is the dynamic viscosity of the fluid, $\dot{\gamma}$ [s^{-1}] is the shear rate, μ_0 [Pa· s] is the minimum viscosity, μ_∞ [Pa· s] is the asymptotic viscosity, τ_0 [Pa] is the apparent yield shear stress and λ [s^{-1}] is the shear stress modifier. These parameters take the following resulting values, as adapted from literature [11,12,14]: $\mu_0 = 0.00309\ Pa\ \cdot s$, $\mu_\infty = 0.002654\ Pa\ \cdot s$, $\tau_0 = 0.00436\ Pa$ and $\lambda = 0.02181\ s^{-1}$.

2.2.2. DISCRETE PHASE

The trajectories of the discrete particles are calculated by integrating the force balance of the particles, which is written out in Equation (6) in a Lagrangian framework. The term on the left side ($m_p \frac{d\overrightarrow{u_p}}{dt}$) represents the total force acting on the particle (with m_p [kg] being the particle mass, and $\frac{d\overrightarrow{u_p}}{dt}$ [m/s²] the first derivative of the particle velocity vector with respect to time, i.e. the particle acceleration). This term equates the separate forces acting on the particle (Newton's second law), given by the gravitational force ($\overrightarrow{F_G}$), the pressure gradient force ($\overrightarrow{F_P}$) and the drag force ($\overrightarrow{F_D}$), respectively.

$$m_p \frac{d\overrightarrow{u_p}}{dt} = \overrightarrow{F_G} + \overrightarrow{F_P} + \overrightarrow{F_D} \quad (6)$$

The gravitational force ($\overrightarrow{F_G}$) is defined as follows:

$$\overrightarrow{F_G} = m_p \vec{g} \frac{(\rho_p - \rho)}{\rho_p} \quad (7)$$

with g [9.81 m/s^2] the gravitational acceleration and ρ_p [kg/m^3] the particle density.

The pressure gradient force ($\overrightarrow{F_P}$) is defined as:

$$\overrightarrow{F_P} = m_p \frac{\rho}{\rho_p} \overrightarrow{u_p}(\nabla \vec{u}) \quad (8)$$

Finally, for the drag force ($\overrightarrow{F_D}$) acting on the particle:

$$\overrightarrow{F_D} = m_p \frac{18\mu}{\rho_p d_p^2} \frac{C_D Re_p}{24} \left(\vec{u} - \overrightarrow{u_p}\right) \quad (9)$$

with d_p the particle diameter [m]. Re_p represents the relative Reynolds number of the particle, which is calculated as:

$$Re_p = \frac{\rho d_p \left|\vec{u} - \overrightarrow{u_p}\right|}{\mu} \quad (10)$$

The drag coefficient, C_D, is derived from the drag law for spherical particles, given by:

$$C_D = a_1 + \frac{a_2}{Re} + \frac{a_3}{Re^2} \quad (11)$$

where Re is the Reynolds number of the fluid and a_1, a_2 and a_3 are constants given in [32].

One-way coupling between the discrete and fluid phase was enabled [19]. The particles were modelled as inert. Particle collisions at the walls were modelled as elastic. No-slip conditions were used at the walls. Particles were injected over the entire inlet plane with a uniform velocity profile approximately equal (<0.5% difference) to the inlet blood flow velocity.

2.2.3. SOLUTION METHODS

For pressure-velocity coupling, the SIMPLE scheme was chosen. The spatial discretization schemes used were Least Squares Cell Based for gradient, Standard for pressure and Second Order Upwind for momentum. An automated particle tracking scheme was chosen which switches automatically between the high order trapezoidal scheme and the low order implicit scheme. For all simulations, absolute globally scaled residuals of at least $2 \cdot 10^{-6}$ were reached.

2.3. BASELINE MODEL

In the baseline model for both livers, particles were modelled as SIR-Spheres (Sirtex Medical, Australia), which are typical treatment particles for TARE. A representative particle diameter (40 µm) and density (1600 kg/m^3) was chosen [19,33].

The inlet boundary condition (BC) was set to a constant flat velocity profile. The inflow in the PHA was determined as a literature-averaged value: Q_{in} = 275.7 ml/min (or 4.595·10-6 m³/s) (see Table 1 for an overview of the studies used). The corresponding inlet velocities were determined as 0.1545 m/s for the HL and 0.1077 m/s for the CL based on the inlet plane surface area. With an inlet plane diameter of 0.00737 m and inlet velocity of 0.1077 m/s (considering $\mu_\infty = 0.002654\ Pa \cdot s$, ρ = 1060 kg/m³,), Re = 317.02, which is well within the laminar regime, justifying the choice for laminar flow.

Outlet BCs were defined using a fractional flow distribution based on Murray's law. This law states that there is a linearity between the flow in a blood vessel and the nth power of the radius of the vessel (R [m]), with n varying between 2 and 3 depending on its size [34]. Considering n=3 because of the small size of the outlets, the following relationship between flow in a parent vessel (Q_{parent} [ml/min]) and flow in a daughter vessel ($Q_{daughter}$ [ml/min]) arises [14,15]:

$$\frac{\mathrm{Q_{daughter}}}{\mathrm{Q_{parent}}} = \left(\frac{\mathrm{R_{daughter}}}{\mathrm{R_{parent}}}\right)^3 \qquad (12)$$

In systems where Murray's law is not perfectly achieved, Equation (12) can be replaced by:

$$\frac{Q_{daughter}}{Q_{parent}} = \left(\frac{R_{daughter}}{\sum_i R_{daughter,i}}\right)^3 \quad (13)$$

The resulting flow split for all outlets of the HL and CL is given in Table 2.

2.4. PARAMETER STUDY

The following parameters were varied with respect to the baseline model: particle diameter, particle density, axial injection location. Compared to the SIR-Spheres for TARE, the typically larger treatment particles for TACE were modelled by a representative diameter of 100 µm (e.g. Tandem particles (Boston Scientific, Massachusetts) [36]). TheraSpheres (also used for TARE) with a density of 3600 kg/m³ were used to estimate the impact of particle density [33]. Three axial injection locations with different distances before the first bifurcation (46.3mm, 30.8 mm and 17.2 mm for the HL; 42.7 mm, 21.6 mm and 11.2 mm for the CL) were tested (Fig. 1). An overview of all simulations with the according injection parameters and particle properties is given in Table 3.

2.5. CANCER BURDEN STUDY

For the cancer burden study, **six** different cancer scenarios were modelled in the CL. The scenarios represent progressive tumor growth, with total tumor volume increasing from 135 ml (low burden) to 564.5 ml (moderate burden) to 1129 ml (high burden). Using Couinaud's classification, the liver was anatomically divided in 8 segments, of which segments 2 and 3, which are perfused by the left hepatic artery, represent the left lobe (LL) and segments 1 and 4-8, which are perfused by the right hepatic artery, representing the right lobe (RL). Two types of cancer scenarios were modelled: tumors constricted to the RL (Case 1-3 in Table 4) and to the LL (Case 4-6). In the RL cases, total tumor tissue was divided over the segments 1 and 4-8, proportionally to the original segment volume. For the LL cases, the tumor tissue was divided

equally over segments 2 and 3. The corresponding total healthy and cancerous volumes of each liver segment are given in Table 4.

The outlet BCs were set according to the arterial perfusion model developed by Aramburu et al. [22]. Knowing the tumor and healthy volume in each segment, the arterial perfusion of each segment can be calculated as the sum of arterial perfusion contributions for the healthy and cancerous tissue. In Aramburu's model [22], an average arterial perfusion constant for cancerous tissue of 0.415 min^{-1} was calculated (based on HCC tumors, metastatic tumors from colorectal carcinomas or metastatic tumors from other primary tumors), compared to 0.10 min^{-1} for healthy tissue. Thus, the arterial perfusion contribution for cancerous tissue is considered to be >4 times higher than for healthy tissue of the same volume. By identifying which branches perfuse which segment and assuming that flow splits occurs symmetrically along bifurcations perfusing the same segment (described by Aramburu et al. [22] as the 'literature-based scenario'), the arterial perfusion of each branch in the domain can be computed and imposed as outlet BC. The branching characteristics of the CL are given in Fig. 1b, and the flow split for each cancer scenario is given in Table 2. More detailed information on the arterial perfusion model can be found in [22]. This method resulted in a total inflow (Q_{in}) of 306 ml/min, 484 ml/min and 718.5 ml/min for low, moderate and high cancer burden, respectively. The corresponding inlet velocities were determined as 0.120 m/s, 0.189 m/s and 0.281 m/s (low to high burden).

2.6. POST-PROCESSING

Particle track files were exported from ANSYS Fluent to CFD-Post (ANSYS, Canonsburg, USA) to visualize particle trajectories and export particle data (i.e. particle destinations and injection locations). Matlab (MathWorks, USA) was used to generate Particle Release Maps (PRMs). PRMs are planar projections of the injection plane that are generated by backtracking

the individual particle trajectories from their exit branches to the injection plane. Hereby, every particle is assigned a color corresponding to its exit branch (see Fig. 1 for examples).

Specific measures were analyzed to compare the particle distribution between different simulations. The particle exit fraction (PEF) denotes the percentage of particles that exit the domain through a specific outlet or larger vascular zone (e.g. outlets draining the right or left lobe). The particle non-exit fraction (PNEF) is the fraction of particles that do not exit the domain. For zone x in a geometry (i.e. a specific outlet or larger vascular zone), the average, minimum and maximum PEF of the 5 different simulations for the parameter study can be calculated, which correspond to the parameters $PEF_{av,x}$, $PEF_{min,x}$ and $PEF_{max,x}$, respectively. The spread in PEF_x over the parameter study ($PEF_{max,x}$ - $PEF_{min,x}$) is an indication of how much the particle distribution in x varies due to alterations in the injection parameters studied. This gives rise to the spread-to-average ratio ($STAR_x$):

$$\mathrm{STAR_x} = \frac{\mathrm{PEF_{max,x}} - \mathrm{PEF_{min,x}}}{\mathrm{PEF_{av,x}}} \qquad (14)$$

A high $STAR_x$ indicates that the PEF_x for a zone x is sensitive towards alterations in the clinical parameters studied. On the other hand, a low $STAR_x$ indicates that the PEF_x is rather stable, and the targeting efficiency for zone x is unlikely to be significantly increased by changing the clinical parameters studied.

2.7. EXPERIMENTAL VALIDATION

As a proof of concept, an in vitro set-up was built to validate the CFD modeling approach by means of an experimental flow circuit using a 3D print. One scenario for the CL was tested in the in vitro set-up in order to study its feasibility and potential for future, more elaborate validation studies.

The 3D simulation geometry of the cirrhotic arterial tree was imported into Magics (Materialise, Leuven, Belgium) to prepare it for 3D printing. More specifically, the geometry (only containing the lumen of the arteries) was hollowed out and an offset thickness of 1.5 mm was added to the outer walls of the domain. Extensions (10-15 mm) were added to the outlets, and their outer diameters were adjusted to facilitate attachment to the downstream tubing. Stereolithography was chosen to manufacture the 3D print using TuskXC2700T material (Materialise, Leuven, Belgium), which is a transparent material that is recommended for use in flow analysis experiments. The resulting 3D print (Fig. 2b) was subsequently mounted in the experimental setup (Fig. 2a, c). The water in the main reservoir (1) was transferred with a DC circular pump (VERDER, The Netherlands) (2) to an elevated reservoir (3). The elevated reservoir was set at a fixed height to mimic the inlet pressure at the PHA (approx. 100 mmHg). When the clamp (4) was released, water flowed down from the reservoir through the 3D-printed geometry (5). The orientation of the 3D print was set in the opposite direction compared to Fig. 1 (i.e. with the outlets oriented downwards), so that gravity would facilitate fluid flow. Polyvinyl chloride (PVC) connecting tubes (6) with tunable resistances (7) were attached to the outlets leading into 10 collecting reservoirs (8). Before releasing particles into the set-up, the boundary conditions were set manually by iteratively adapting the resistances at the PVC tubes until all outflows matched the computational boundary conditions (< 5% error margin). More specifically, the resistances were set according to a cancer-free scenario according to Aramburu's arterial perfusion model (Table 4).

Non-radioactive SIR-Spheres (Sirtex Medical, Australia) were mixed with water in the main reservoir for the first experiment. During the second experiment, particles were manually injected with a syringe via side-branch of the inlet branch leading to the PHA and then flushed with water. The 21 outlets were combined in 10 collecting reservoirs (see Fig. 2a, c) and the resulting particle-water mixture was collected in these reservoirs for a total duration of 1 minute

starting from the moment of injection. Whatman paper of grade 2 and 3 (pore size 8 and 6 µm, respectively) was used to filter the particles from the collected particle-water mixtures. After drying, the filters were weighed to determine the added weight of the particles, and hence, the particle distribution among the collecting reservoirs. The PNEF could not be considered in these experiments (the sum of all PEFs at the outlets was assumed to be 100% of the particles). In order to allow comparing the experimental results to the CFD modeling approach, an additional CFD simulation was performed on the CL in order to replicate the experimental conditions outlined above (e.g. using fluid properties of water instead of blood).

3. RESULTS

3.1. BASELINE MODELS

In the HL baseline model, 51.33% of the particles flow to the right lobe (RL), while a smaller fraction (37.33%) flows to the left lobe (LL) (Fig. 3a). The CL shows the same trend with a smaller fraction of particles flowing to the LL (22.70%) compared to the RL (66.00%) (Fig. 3b). The PNEF is similar for both livers: 11.35% and 11.30% for the HL and CL, respectively.

Fig. 4a shows the PRMs for the HL and CL baseline models. For the HL, releasing particles in the blue region of the PRM (outlets 1-8) leads to particle transport towards the RL, while particles exiting the LL originate from the complementary moon-shaped region (outlets 9-16). For the CL, releasing particles in the red U-shaped region (outlets 17-21) leads to particle deposition in the LL. Particles exiting the RL originate from the oval-shaped region at the center of the PRM (outlets 1-16). Non-exiting particles (represented by black dots) were smeared out over the PRMs for both the HL and CL. Note that the thicker side of the LL injection region is located at the left periphery of the PRM in Fig. 4a, while the LL itself is located at the right side of the PRM (patient view, see Fig. 1b).

3.2. PARAMETER STUDY

3.2.1. IN-PLANE INJECTION LOCATION

Fig. 4a clearly illustrates the significant impact of the in-plane injection location on the particle fate, showing potential for targeting individual outlets or zones. According to the HL and CL PRMs, particle injections near the bottom wall may result in a significant fraction of particles getting stuck in the domain.

3.2.2. PARTICLE SIZE AND DENSITY

For the HL, the PEF_{RL} decreases from 51.33% (baseline) to 40.62% and 42.21% for the particles with a larger diameter (bigger) and density (denser), respectively. The PEF_{LL} decreases from 37.33% to 22.48% (bigger) and 26.30% (denser) (Fig. 3a). The PNEF increases from 11.35% in the baseline model to 36.90% (bigger) and 31.50% (denser).

For the CL, the PEF_{RL} decreases from 66% (baseline) to 47.42% (bigger) and 52.75% (denser) for the particles with a larger diameter and density, respectively. Concurrently, the PEF_{LL} decreases from 22.70% (baseline) to 14.40% (bigger) and 16.39% (denser) (Fig. 3b). The PNEF increases from 11.30% (baseline) to approximately the threefold, i.e. 38.18% (bigger) and 30.86% (denser) (see also more non-exiting particles in Fig. 4a).

3.2.3. AXIAL INJECTION LOCATION

For the HL, the PEF_{RL} decreases from 51.33% to 43.85% (middle) and 44.55% (close), while the PEF_{LL} increases from 37.33% to 41.91% (middle) and 42.89% (close) (Fig. 3a). The PNEF increases from 11.35% (baseline) to 14.24% (middle) and 12.56% (close). The difference in outlet-specific PEFs compared to the baseline is maximal in LL outlet 12 for both the middle and close injection plane (3.84% and 2.77% increase, respectively). The PEF difference is smallest for LL outlet 13 (0.12% increase) and RL outlet 1 (0.07% decrease) for the middle and close injection location, respectively.

For the CL, the PEF_{RL} decreases from 66% (baseline) to 51.31% and 55.61% for the middle and close injection locations, respectively (Fig. 3b). Concurrently, the PEF_{LL} increases from 22.70% (baseline) to 32.06% (middle) and 30.43% (close). The PNEF increases from 11.30% (baseline) to 16.63% (middle) and 13.97% (close). The difference in outlet-specific PEFs compared to the baseline is highest in LL outlets 21 (4.57% increase) and 17 (3.47% increase) for the middle and close injection plane, respectively. The PEF difference is smallest in RL outlet 7 (0.12% and 0.06% decrease for the middle and close injection planes, respectively).

Both livers also showed changes in the shape and pattern of the PRMs when changing axial injection location (Fig. 4a).

3.3. CANCER BURDEN STUDY

When increasing the LL cancer burden in the CL (O17-21), the PEF_{LL} is 32.11% (low burden), 49.76% (moderate burden) and 58.16% (high burden) (Fig. 5a). For increasing the RL cancer burden (O1-16), the PEF_{RL} is 72.25% (low), 76.67% (moderate) and 79.60% (high) (Fig. 5b). From the PRMs in Fig. 4b, it is clear that the in-plane targeting region for the LL largely increases for increasing LL cancer burden. A similar effect occurs for increasing RL cancer burden, but the increase is less noticeable.

3.4. EXPERIMENTAL VALIDATION

In Fig. 2d, the flow distribution and particle fraction for each reservoir (reservoir exit fraction, or REF) was compared for the 2 experiments and the corresponding numerical simulation. The high similarity between experimental and theoretical flow distribution (0.407% difference per reservoir on average) shows that the implementation of the outlet BCs through tuning of the resistances was successful. However, after particle injection, the average difference per reservoir between experimental PD and FD was 2.45% (min: 0.0784% - max: 5.44%) and 2.14% (min: 0.902% - 4.03%) for experiment 1 and 2, respectively. Moreover, the average

difference for a reservoir between numerical and experimental PD was 2.73% (min: 0.394% - max: 6.47%) and 2.97% (min: 1.21% - max: 6.17%) for experiment 1 and 2, respectively.

4. DISCUSSION

In this study, we investigated the impact of several clinical parameters on the PD, and the feasibility of using these parameters to steer particles towards specific vascular zones starting from injections in the PHA.

Judging the impact of particle size and density (Fig. 3 and 4a) is challenging due to the ambiguous interpretation of the PNEF. Assuming tumor nodules are small and located downstream of the domain outlets, the PNEF represents extra offsite toxicity, because the particles do not exit the tumor-perfusing outlets. In these cases, injections with bigger or denser particles is deemed unideal. However, there could be more advanced cancer scenarios where the PNEF does not necessarily represent extra offsite toxicity (e.g. if the entirety of the right lobe is cancerous and, hence, targeted). Considering only exiting particles, injections with bigger and denser particles shift the PEF slightly towards the RL (by respectively 3.7% and 6.5% for the HL, and 1.9% and 2.3% for the CL). These small differences seem to illustrate the rather limited targeting potential of particle size and density. The same was concluded by Aramburu et al. [24] for their patient-specific geometry.

Shifting the catheter closer towards the bifurcation at the end of the PHA increased the PEF_{LL} in both geometries by up to 6% in the HL, and 10% in the CL (Fig. 3 and 4a). This trend also agrees with Aramburu et al. [21], where it was stated that injecting near or far away from a bifurcation has a significant impact on the PD.

The PRMs in Fig. 4 show that in-plane control of the catheter tip position may enable steering particles towards specific outlets of the vasculature, which agrees with [11,12,18–24,27]. In theory, limiting the catheter tip to a specific zone could increase the target specificity to 100%.

However, the main limitations of this method are that the PRMs should still be thoroughly validated in vivo/in vitro, and that it remains unknown whether careful control of the in-plane catheter tip position is realistically achievable during the procedure. When the latter is not possible, parameter optimization can play an important role in maximizing targeting for specific outlets. For example, the panels for the CL in Fig. 4a show that the targeting zone for outlet 14 (yellow) is significantly smaller for bigger particles than for the baseline model. For this specific patient, this could be an incentive to prefer injection with particles with a smaller size.

Generally, the targeting potential of each geometry can be interpreted by means of the STAR. The $STAR_{RL}$ is 0.24 (spread of 10.72%) and 0.34 (spread of 18.6%) for the HL and CL, respectively. The $STAR_{LL}$ is 0.60 (spread of 20.41%) and 0.76 (spread of 17.66%) for the HL and CL, respectively. This shows that the LLs have a higher targeting potential than their respective RLs. Averaged over all outlets, the STAR is 0.483 (min: 0.178 – max: 1.35) and 0.549 (min: 0.06–max: 1.49) for the CL and HL. Combining all of the above, it can be concluded that the targeting potential varies between vascular zones (higher for the LL than RL, and different from outlet to outlet), patient-specific geometries (slightly higher for the CL than HL) and the choice of parameters (higher for axial and in-plane injection location than for particle properties).

Considering the impact of cancer burden on the PRMs, the targeting zones grow for higher cancer burden (Fig. 4b). However, this effect is highly heterogeneous and dependent on patient-specific conditions. For example, the growth of targeting zones for a higher LL cancer burden was much more significant than for a higher RL cancer burden, probably due to the larger initial size of the RL. Nonetheless, targeting the RL in a cancer scenario with tumor nodules confined to the RL should be feasible by injection in the PHA, since the targeting zone compromised nearly the entire arterial cross-section. These results agree with Aramburu et al. [12], stating that targeting should become easier as cancer burden grows. However, it should also be noted

that drug delivery inside the tumor is likely to be more difficult for higher cancer burden (high tumor mass density, high interstitial pressure, abnormal vasculature etc. [37].

Overall, injection before the first bifurcation in the PHA may be a suitable injection method in some cases, for example high cancer burden in the RL as outlined above. In other cases, a combination of parameter optimization, including precise control of in-plane catheter tip location, and catheter advancement beyond the first bifurcation can significantly increase the target specificity of the procedure, although the suitability of each method is highly geometry- and patient-specific. Note that the observations presented here were made based upon two patient-specific datasets and cannot be generalized.

Since Simoncini et al. [26] and Roncali et al. [25] reasoned that PD is linearly proportional with the FD, the similarity between FD and PD is useful to consider. In the validation study and numerical results, it was shown that FD is not a perfect surrogate for PD, at least not for the complex patient-specific livers studied (Fig. 2d). Note that FD also does not consider the non-exiting particles, which may be relevant because these can contribute to offsite toxicity. Hence, PD should also be studied if possible. A second important observation was that there are still significant differences between the computational and in vitro PD (Fig. 2d), emphasizing the need for further validation and finetuning of methods.

There are several limitations to the research, which – at the same time – inspire future work. First, two types of outlet BCs were used: (i) Murray's law, and (i) the perfusion methodology [22], while neither has been validated in vivo yet. Note that in Table 2 two sets of outlet BCs were reported for a cancer-free scenario in the CL (according to the 2 types of BCs). This discrepancy stresses that, moving forward, more appropriate BCs should ideally be used, preferably validated by or based on patient-specific in vivo measurements. Second, from a modeling perspective, the effect of transient cardiac pulses should ideally be included to more accurately describe the PD in physiological conditions (i.e. for particle release during a

specified, clinically achievable time window) [11,19]. Importantly, more attention should be paid to the clinical interpretation of the non-exit particles in these transient conditions. Third, it should be noted that geometries generated from vascular corrosion casting can be slightly expanded compared to in vivo conditions, but that shrinkage of the resin can also occur [38]. In the future, the use of patient-specific anatomical imaging resulting from CT or MRI scans should be prioritized. Fourth, the scope of this study was limited to studying uncontrolled particle injection in the PHA in two patient-specific geometries. In addition to the parameters studied in this work, other clinically relevant parameters (such as injection velocity, catheter type, catheter tip orientation, etc.) should also be studied to fully estimate the possibilities offered by parameter optimization [11,12,14,20,21]. Future work also should focus on modelling axial injection locations beyond the first bifurcation, up to the point where the vasculature becomes inaccessible for catheters. As such, the workflow proposed in this study can be repeated for this larger range of axial locations to investigate the impact of parameter optimization for injection further downstream. Similarly, injections with more precise control of in-plane catheter tip location should be studied. Overall, more patient-specific liver geometries should be studied to verify the observations made. Last but not least, the scope of the experimental study was currently limited to a proof-of-concept, but should be expanded to investigate the sensitivity of the experimental PDs towards varying injection conditions and particle parameters.

5. CONCLUSIONS

For two patient-specific liver geometries, the impact of several parameters on the PD throughout the liver vasculature during transarterial therapies was studied both numerically and experimentally. Axial and in-plane injection locations have a large impact on the particle distribution, which can be used to steer particles towards specific exit branches. Large particle sizes and densities mainly increase the particle non-exit fraction. The healthy and cirrhotic

geometry clearly differ in PD, injection plane targeting zones (according to the PRMs) and the impact of clinical parameters on the PD. For increasing cancer burden, the in-plane location of the catheter tip matters less, but this effect is very patient-specific. Experimental validation confirmed that the FD is not a perfect surrogate for PD. In conclusion, a combination of parameter optimization, catheter advancement and catheter tip control may enable increasing the target specificity for particle delivery during patient-specific transarterial treatments for liver cancer.

6. ACKNOWLEDGEMENTS

We would like to thank Sirtex Medical for the delivery of experimental SIR-Spheres for the in vitro validation study.

The research was supported by the special research fund, Ghent University (grant number BOFSTA201909015). Charlotte Debbaut was partially supported by a postdoctoral fellowship from Research Foundation Flanders (1202418N).

7. AUTHOR CONTRIBUTIONS

Tim Bomberna, Ghazal Adeli Koudehi, Charlotte Claerebout and Charlotte Debbaut were involved in study conception and design. Tim Bomberna, Ghazal Adeli Koudehi, and Charlotte Debbaut were involved in analysis and interpretation of the data. Tim Bomberna and Charlotte Debbaut were involved in paper drafting and revision. Geert Maleux and Chris Verslype were involved in data collection, paper revision and provided clinical input. All authors agree to be accountable for all aspects of the work.

8. REFERENCES

[1] Villanueva A. Hepatocellular carcinoma. N Engl J Med. 2019;380(15):1450–1462.

[2] Balogh J, Victor D, III, Gordon S, et al. Hepatocellular carcina: a review. J Hepatocell Carcinoma. 2016;3:41–53.

[3] Tang A, Hallouch O, Chernyak V, et al. Epidemiology of hepatocellular carcinoma: target population for surveillance and diagnosis. Abdom Radiol. 2018;43(1): 13–25.

[4] Savitha G, Vishnupriya V, Krishnamohan S. Hepatocellular carcinoma- A review. J Pharm Sci Res. 2017;9(8):1276–1280.

[5] Lencioni R, Petruzzi P, Crocetti l. Chemoembolization of hepatocellular carcinoma. Semin Intervent Radiol. 2013;30(1): 3–11.

[6] Salem R, Lewandowski RJ. Chemoembolization and radioembolization for hepatocellular carcinoma. Clin Gastroenterol Hepatol. 2013;11(6): 604–611.

[7] Mosconi C, Cappelli A, Pettinato C, et al. Radioembolization with Yttrium-90 microspheres in hepatocellular carcinoma: Role and perspectives. World J Hepatol. 2015;7(5):738–752.

[8] Lewis AL, Dreher MR. Locoregional drug delivery using image-guided intra-arterial drug eluting bead therapy. J Control Release. 2012;161(2): 338–350.

[*9] Peeters G, Debbaut C, Cornillie P, et al. A multilevel modeling framework to study hepatic perfusion characteristics in case of liver cirrhosis. J Biomech Eng. 2015;137(5):pages.

*** An important original research paper studying hepatic perfusion in liver cirrhosis, serving as a precursor to this paper, which studies particle delivery in a patient with liver cirrhosis**

[10] Sacco R, Tapete G, Simonetti N. Transarterial chemoembolization for the treatment of hepatocellular carcinoma: a review. J Hepatocell Carcinoma. 2017;27(4):105-110.

[11] Kleinstreuer C, Basciano CA, Childress EM, et al. A new catheter for tumor targeting with radioactive microspheres in representative hepatic artery systems. Part I: Impact of catheter presence on local blood flow and microsphere delivery. J Biomech Eng. 2012;134(5):1–10.

[12] Aramburu J, Antón R, Rivas A, et al. Computational particle–haemodynamics analysis of liver radioembolization pretreatment as an actual treatment surrogate. Int J Numer Method Biomed Eng. 2017;33(2):1–18.

[13] Childress EM, Kleinstreuer C. Impact of fluid-structure interaction on direct tumor-targeting in a representative hepatic artery system. Ann Biomed Eng. 2014;42(3):461–474.

[14] Aramburu J, Antón R, Rivas A, et al. The role of angled-tip microcatheter and microsphere injection velocity in liver radioembolization: A computational particle–hemodynamics study. Int J Numer Method Biomed Eng. 2017;33(12):1–16.

[15] Kleinstreuer C. Drug-targeting methologies with applications: A review. World J Clin Cases. 2014;2(12):742–756.

[16] Longest PW, Bass K, Dutta R, et al. Use of computational fluid dynamics deposition modeling in respiratory drug delivery. Expert Opin. Drug Delivery. 2018;16(1):7–26.

[17] Ehrmann S, Schmid O, Darquenne C, et al. Innovative preclinical models for pulmonary drug delivery research. Expert Opin. Drug Delivery. 2020;17(4):463–478.

[18] Kennedy AS, Kleinstreuer C, Basciano CA, et al. Computer Modeling of Yttrium-90-Microsphere Transport in the Hepatic Arterial Tree to Improve Clinical Outcomes. Int J Radiat Oncol Biol Phys. 2010;76(2):631–637.

[19] Basciano CA, Kleinstreuer C, Kennedy AS, et al. Computer modeling of controlled microsphere release and targeting in a representative hepatic artery system. Ann Biomed Eng. 2010;38(5):1862–1879.

[20] Childress EM, Kleinstreuer C, Kennedy AS. A new catheter for tumor-targeting with radioactive microspheres in representative hepatic artery systems-Part II: Solid tumor-targeting in a patient-inspired hepatic artery system. J Biomech Eng. 2012;134(5).

[21] Aramburu J, Antón R, Rivas A, et al. Computational assessment of the effects of the catheter type on particle–hemodynamics during liver radioembolization. J Biomech. 2016;49(15):3705–3713.

[*22] Aramburu J, Antón R, Rivas A, et al. Liver cancer arterial perfusion modelling and CFD boundary conditions methodology: a case study of the haemodynamics of a patient-

specific hepatic artery in literature-based healthy and tumour-bearing liver scenarios. Int J Numer Method Biomed Eng. 2015;32(11). *** An important original research paper detailing the boundary conditions methodology as similarly used in this study.**

[23] Oktar SÖ, Yücel C, Demirogullari T, et al. Doppler Sonographic Evaluation of Hemodynamic Changes in Colorectal Liver Metastases Relative to Liver Size. J Ultrasound Med. 2006;25(5):575–582.

[*24] Aramburu J, Antón R, Rivas A, et al. Liver Radioembolization: An Analysis of Parameters that Influence the Catheter-Based Particle-Delivery via CFD. Curr Med Chem. 2020;27(10):1600-1615. *** An important review paper overviewing the state of research regarding the impact of clinical parameters on particle distribution.**

[25] Roncali E, Taebi A, Foster C, et al. Personalized Dosimetry for Liver Cancer Y-90 Radioembolization Using Computational Fluid Dynamics and Monte Carlo Simulation. Ann Biomed Eng. 2020;48(5):1499–1510.

[26] Simoncini C, Jurczuk K, Reska D, et al. Towards a patient-specific hepatic arterial modeling for microspheres distribution optimization in SIRT protocol. Med Biol Eng Comput. 2018;56(3):515–529.

[27] Aramburu J, Antón R, Rivas A, et al. Numerical investigation of liver radioembolization via computational particle–hemodynamics: The role of the microcatheter distal direction and microsphere injection point and velocity. J Biomech. 2016;49(15):3714–3721.

[28] Peeters C, Debbaut C, Friebel A, et al. Quantitative analysis of hepatic macro- and microvascular alterations during cirrhogenesis in the rat. J Anat. 2018;232(3):485–496.

[29*] Debbaut C, Segers P, Cornillie P, et al. Analyzing the human liver vascular architecture by combining vascular corrosion casting and micro-CT scanning: a feasibility study. J Anat.

2014;224(4):509-517. *** An important paper detailing the vascular corrosion casting and micro-CT scanning technique which generated the 2 patient-specific domains used in this study**

[30] Peeters G. Numerical Simulations for Assessment of the Hepatic Microcirculatory Hemodynamics in Human Cirrhosis [master's thesis]. Ghent: Ghent University; 2013.

[31] Buchanan JR, Kleinstreuer C, Comer JK. Rheological effects on pulsatile hemodynamics in a stenosed tube. Comput Fluids. 2000;29(6):695–724.

[32] Morsi SA, Alexander AJ. An investigation of particle trajectories in two-phase flow systems. J Fluid Mech. 1972;55(2):193–208.

[33] Murthy R, Kamat P, Nunez R, et al. Radioembolization of yttrium-90 microspheres for hepatic malignancy. Semin Intervent Radiol. 2008;25(1):48–57.

[34] Revellin R, Rousset F, Baud D, et al. Extension of murray's law using a non-newtonian model of blood flow. Theor Biol Med Model. 2009;6(1):7.

[35] Sherman TF. On connecting large vessels to small. J Gen Physiol. 1981;78(4):431–453.

[36] de Baere T, Plotkin S, Yu R. An In Vitro Evaluation of Four Types of Drug-Eluting Microspheres Loaded with Doxorubicin. J Vasc Interv Radiol. 2016;27(9):1425–1431.

[37] Jang SH, Wientjes MG, Lu D, et al. Drug delivery and transport to solid tumors. Pharm Res. 2003;20(9):1337–1350.

[38] Kratky RG, Roach MR. Shrinkage of Batson's and its relevance to vascular casting. Atherosclerosis. 1984;51(2–3):339–341.

[39] Carlisle KM, Halliwell M, Read AE, et al. Estimation of total hepatic blood flow duplex ultrasound. Gut. 1992;33(1):92–97.

[40] Zoli M, Magalotti D, Bianchi G, et al. Total and functional hepatic blood flow decrease in parallel with ageing. Age Ageing. 1999;28(1): 29–33.

[41] Săftoiu A, Ciurea T, and Gorunescu F. Hepatic arterial blood flow in large hepatocellular carcinoma with or without portal vein thrombosis: Assessment by transcutaneous duplex Doppler sonography. Eur J Gastroenterol Hepatol. 2002;14(2):167–176, 2002.

[42] Yzet T, Bouzerar R, Allart J-D, et al. Hepatic vascular flow measurements by phase contrast MRI and doppler echography: a comparative and reproducibility study. J Magn Reson Imaging. 2010;31(3):579–588.

INDICATION OF TABLES

TABLES

Table 1

Number of patients	Measurement method	Source	Mean flow (ml/min)
10	Duplex Doppler US	Carlisle et al. [39]	212 ± 75
10	Eco Doppler US	Zoli et al. [40]	235 ± 76
10	Eco Doppler US	Zoli et al. [40]	313 ± 117
10	Eco Doppler US	Zoli et al. [40]	318 ± 144
10	Eco Doppler US	Zoli et al. [40]	271 ± 94
30	Duplex Doppler US	Saftoiu et al. [41]	224 ± 56
9	PC-MRI	Yzet et al. [42]	215 ± 101
9	Doppler US	Yzet et al. [42]	541.5 ± 272
Total sample size		Average mean flow (ml/min)	
98		275.7	

Table 2

Outlet	Boundary condition: Murray's law		Boundary condition: Aramburu's perfusion model (only for the cirrhotic liver)						
	Healthy liver	Cirrhotic liver	No cancer scenario	Cancer case 1	Cancer case 2	Cancer case 3	Cancer case 4	Cancer case 5	Cancer case 6
1	7.89%	10.73%	0.86%	0.94%	1.08%	1.15%	0.71%	0.44%	0.30%
2	6.74%	3.10%	0.86%	0.94%	1.08%	1.15%	0.71%	0.44%	0.30%
3	5.71%	2.01%	0.43%	0.47%	0.54%	0.57%	0.35%	0.22%	0.15%
4	4.12%	6.19%	0.43%	0.47%	0.54%	0.57%	0.35%	0.22%	0.15%
5	11.0%	3.84%	0.86%	0.94%	1.08%	1.15%	0.71%	0.45%	0.30%
6	4.24%	2.88%	3.46%	3.78%	4.31%	4.60%	2.82%	1.78%	1.20%
7	9.43%	1.32%	6.91%	7.56%	8.61%	9.21%	5.65%	3.57%	2.40%
8	9.00%	5.27%	6.40%	6.46%	6.55%	6.60%	5.23%	3.31%	2.23%
9	10.24%	3.44%	6.63%	6.85%	7.21%	7.41%	5.42%	3.42%	2.31%
10	2.30%	5.18%	6.63%	6.85%	7.21%	7.41%	5.42%	3.42%	2.31%
11	4.12%	8.98%	8.54%	8.90%	9.49%	9.82%	6.97%	4.41%	2.97%
12	5.81%	8.81%	8.03%	8.47%	9.19%	9.60%	6.56%	4.14%	2.79%
13	5.10%	7.64%	13.26%	13.70%	14.42%	14.82%	10.83%	6.85%	4.62%
14	7.14%	6.42%	8.54%	8.90%	9.49%	9.82%	6.97%	4.41%	2.97%
15	4.07%	1.92%	4.07%	3.87%	3.54%	3.36%	3.32%	2.10%	1.41%
16	3.09%	0.86%	6.40%	6.46%	6.55%	6.60%	5.23%	3.31%	2.23%
17	-	6.37%	4.02%	3.28%	2.07%	1.40%	7.86%	14.17%	17.70%
18	-	2.02%	2.41%	1.97%	1.24%	0.84%	4.26%	7.29%	8.99%
19	-	2.50%	2.41%	1.97%	1.24%	0.84%	4.26%	7.29%	8.99%
20	-	1.22%	4.83%	3.94%	2.49%	1.68%	8.52%	14.59%	17.98%
21	-	9.33%	4.02%	3.28%	2.07%	1.40%	7.85%	14.17%	17.70%

Table 3

Simulation	Geometry	Particle diameter (μm)	Particle density (kg/m^3)	Injection plane	Injection velocity (m/s)
1	Healthy	40	1600	Inlet	0.155
2	Healthy	100	1600	Inlet	0.155
3	Healthy	40	3600	Inlet	0.155
4	Healthy	40	1600	Middle	0.154
5	Healthy	40	1600	Close	0.154
6	Cirrhotic	40	1600	Inlet	0.108
7	Cirrhotic	100	1600	Inlet	0.108
8	Cirrhotic	40	3600	Inlet	0.108
9	Cirrhotic	40	1600	Middle	0.108
10	Cirrhotic	40	1600	Close	0.108

Table 4

Liver segment	Healthy segment volume						
		Right lobe			Left lobe		
		CASE 1	CASE 2	CASE 3	CASE 4	CASE 5	CASE 6
		Low burden [ml]	Moderate burden [ml]	High burden [ml]	Low burden [ml]	Moderate burden [ml]	High burden [ml]
1	101.63	4.02	16.83	33.65	0	0	0
2	200.71	0	0	0	67.5	282.25	564.5
3	241.36	0	0	0	67.5	282.25	564.5
4	345.53	28.17	117.78	235.56	0	0	0
5	320.12	18.11	75.71	151.43	0	0	0
6	200.71	14.08	58.89	117.78	0	0	0
7	426.83	28.37	118.62	237.24	0	0	0
8	663.11	42.25	176.67	353.34	0	0	0

INDICATION OF FIGURES

Figure 1: Illustrations of the simulation geometries. 3D models of the arterial network of the (A) healthy liver and (B) cirrhotic liver. The three axial injection locations used for the parameter study are indicated. The particle release map (PRM) of the baseline model is also shown with respect to the model orientation. The colored sections of the PRM show through which branches the particles exit if they are injected in that specific section (see color bar). Particles that don't exit the domain are denoted in black. Schematic 2D representation of the branching topology of the (A) healthy liver with 16 outlets and (B) the cirrhotic liver with 21 outlets.

Figure 2: Experimental in vitro set-up and results. (A) schematic representation of the set-up. 1: main reservoir. 2: DC pump. 3: Elevated water reservoir. 4: Clamp. 5: 3D printed liver geometry (cirrhotic). 6: PVC connecting tubes. 7: Collecting reservoirs. (B) Overview of the set-up, showing the 3D model, the PVC tubing attached to the outlets, the resistances used to tune the flow distribution and the collection reservoirs. (C) Experimental set-up in the lab, showing the 3D model of the liver vasculature, the elevated reservoir and the collecting reservoirs at the outlets. (D) Results of the validation study. The experimental and theoretical flow distribution (FD) are compared with the particle distributions (PD) for Experiment 1 and 2, and the numerical simulation.

Figure 3: Particle exit fractions (PEFs) for the 5 scenarios of the parameter study. PEFs are reported for in both geometries, being (A) the healthy liver and (B) the cirrhotic liver (left to right: baseline, higher diameter, higher density, middle injection location, close injection location). The total particle fractions exiting the left (O17-O21 for the cirrhotic liver, O9-16 for the healthy liver) and right lobe (O1-16 for the cirrhotic liver, O1-O8 for the healthy liver) are

given above the bars. The non-exit fraction (Outlet “0”) is largest for the bigger and denser particles.

Figure 4: Particle release maps (PRMs) of the computational simulations. (A) PRMs for the parameter study of both the healthy and cirrhotic liver. For the healthy liver, injection in the blue section (O1-8) leads to particle deposition in the right lobe, while injection in the complementary moon-shaped section (O9-16) leads to deposition in the left lobe. For the cirrhotic liver, injection in the red section (O17-21) leads to particle deposition in the left lobe, while injection in the complementary section (O1-16) leads to deposition in the right lobe. (B) PRMs for the cancer burden study in the cirrhotic liver. Top row: tumors in left lobe with growing burden. Bottom row: PRMs for tumors in right lobe with growing burden (left to right: low to high).

Figure 5: Particle exit fractions for varying cancer burden. Particles which do not exit the domain are denoted by Outlet “0”. (A) For growing tumor burden in the left lobe, the number of particles depositing in the left lobe increases significantly. (B) For growing tumor burden in the right lobe, the number of particles depositing in the right lobe increases, but not as significantly.

FIGURES

Figure 1

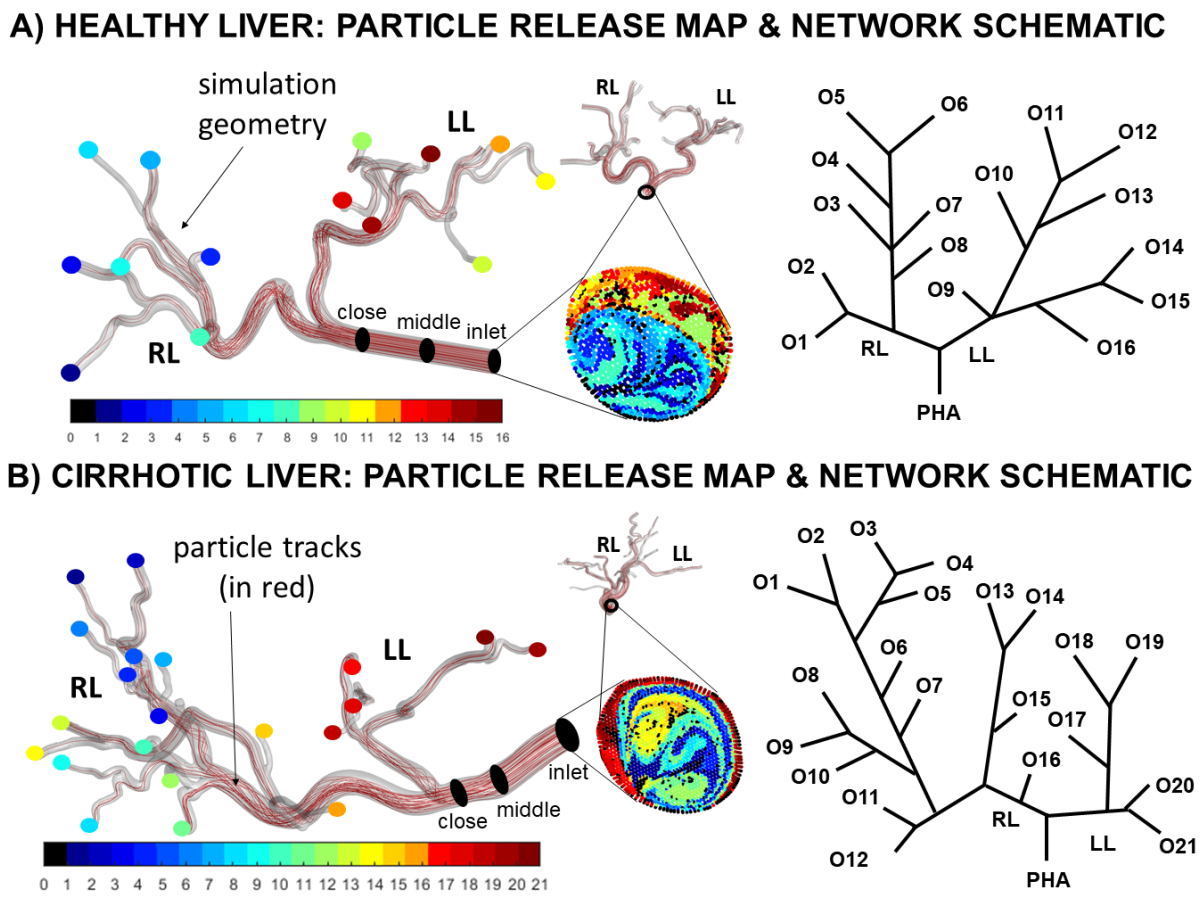

Figure 2

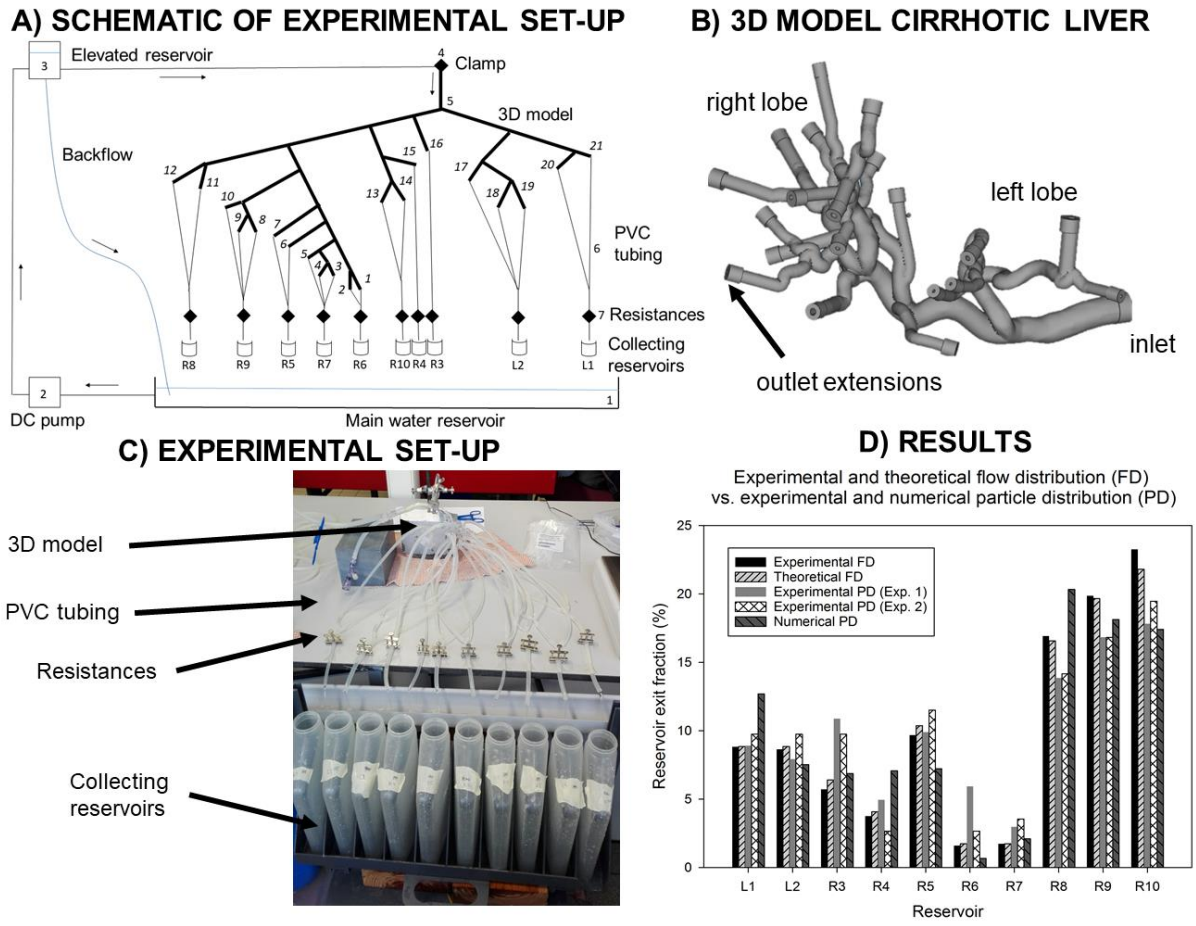
A) SCHEMATIC OF EXPERIMENTAL SET-UP
Elevated reservoir
Clamp
3D model
Backflow
PVC tubing
Resistances
Collecting reservoirs
R8 R9 R5 R7 R6 R10 R4 R3 L2 L1
DC pump
Main water reservoir
B) 3D MODEL CIRRHOTIC LIVER
right lobe
left lobe
inlet
outlet extensions
C) EXPERIMENTAL SET-UP
3D model
PVC tubing
Resistances
Collecting reservoirs
D) RESULTS
Experimental and theoretical flow distribution (FD)
vs. experimental and numerical particle distribution (PD)
Experimental FD
Theoretical FD
Experimental PD (Exp. 1)
Experimental PD (Exp. 2)
Numerical PD
Reservoir exit fraction (%)
Reservoir
L1 L2 R3 R4 R5 R6 R7 R8 R9 R10

Figure 3

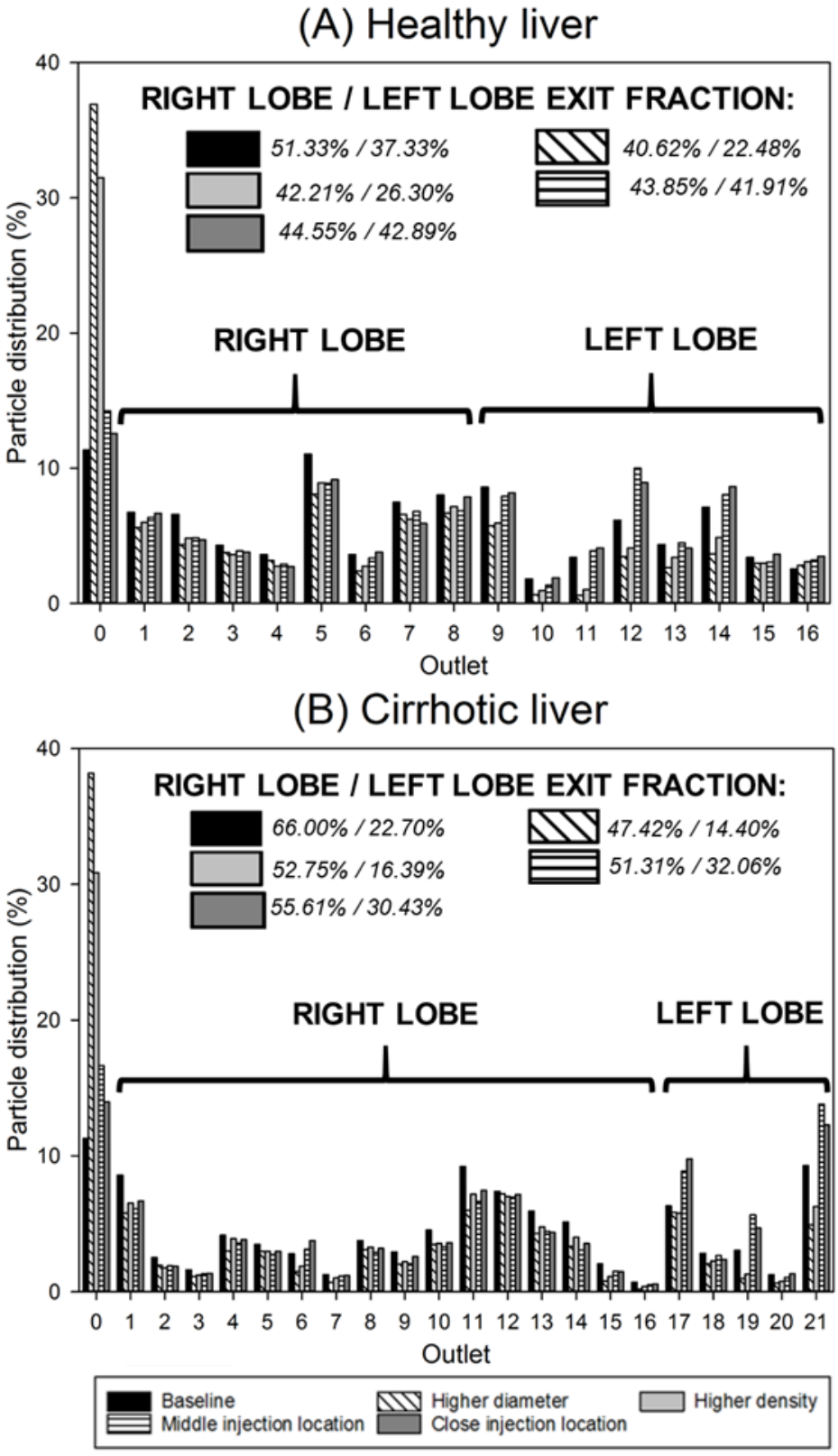
(A) Healthy liver
RIGHT LOBE / LEFT LOBE EXIT FRACTION:
51.33% / 37.33%
42.21% / 26.30%
44.55% / 42.89%
40.62% / 22.48%
43.85% / 41.91%
RIGHT LOBE
LEFT LOBE
Particle distribution (%)
Outlet
(B) Cirrhotic liver
RIGHT LOBE / LEFT LOBE EXIT FRACTION:
66.00% / 22.70%
52.75% / 16.39%
55.61% / 30.43%
47.42% / 14.40%
51.31% / 32.06%
RIGHT LOBE
LEFT LOBE
Particle distribution (%)
Outlet
Baseline
Middle injection location
Higher diameter
Close injection location
Higher density

Figure 4

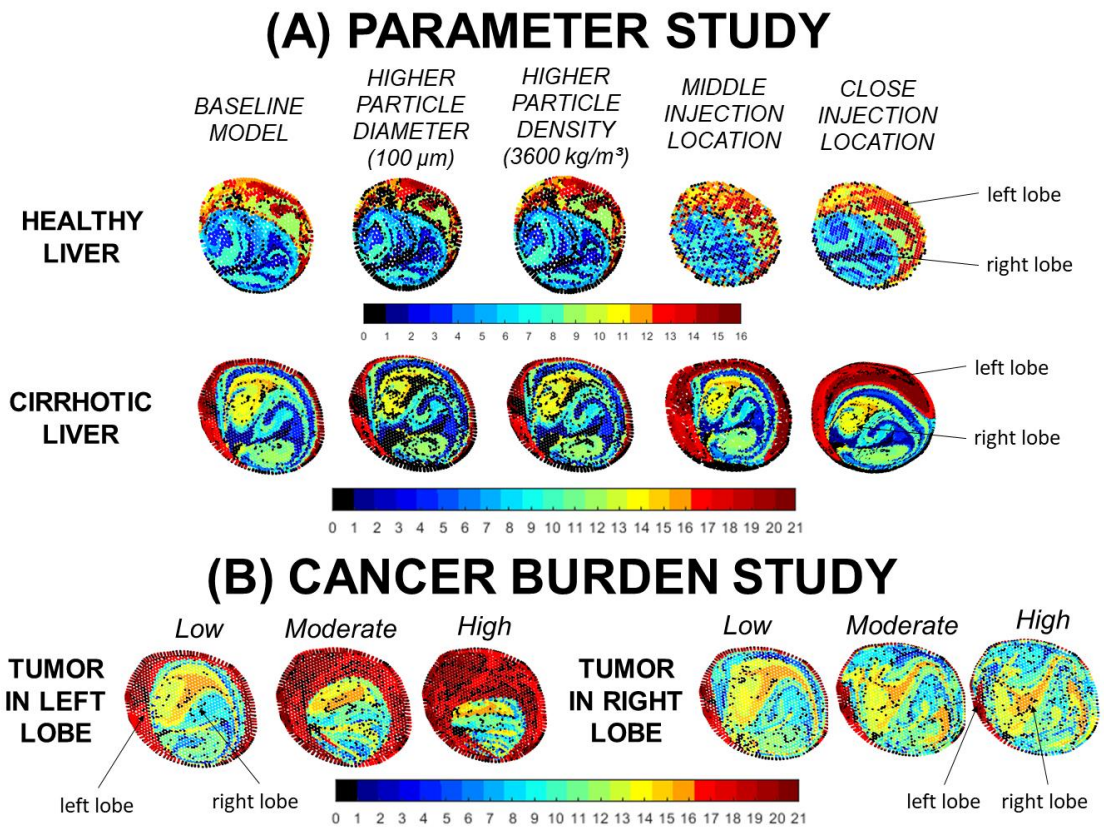
(A) PARAMETER STUDY
BASELINE MODEL
HIGHER PARTICLE DIAMETER (100 μm)
HIGHER PARTICLE DENSITY (3600 kg/m³)
MIDDLE INJECTION LOCATION
CLOSE INJECTION LOCATION
HEALTHY LIVER
left lobe
right lobe
0 1 2 3 4 5 6 7 8 9 10 11 12 13 14 15 16
CIRRHOTIC LIVER
left lobe
right lobe
0 1 2 3 4 5 6 7 8 9 10 11 12 13 14 15 16 17 18 19 20 21
(B) CANCER BURDEN STUDY
Low
Moderate
High
TUMOR IN LEFT LOBE
left lobe
right lobe
Low
Moderate
High
TUMOR IN RIGHT LOBE
left lobe
right lobe
0 1 2 3 4 5 6 7 8 9 10 11 12 13 14 15 16 17 18 19 20 21

Figure 5

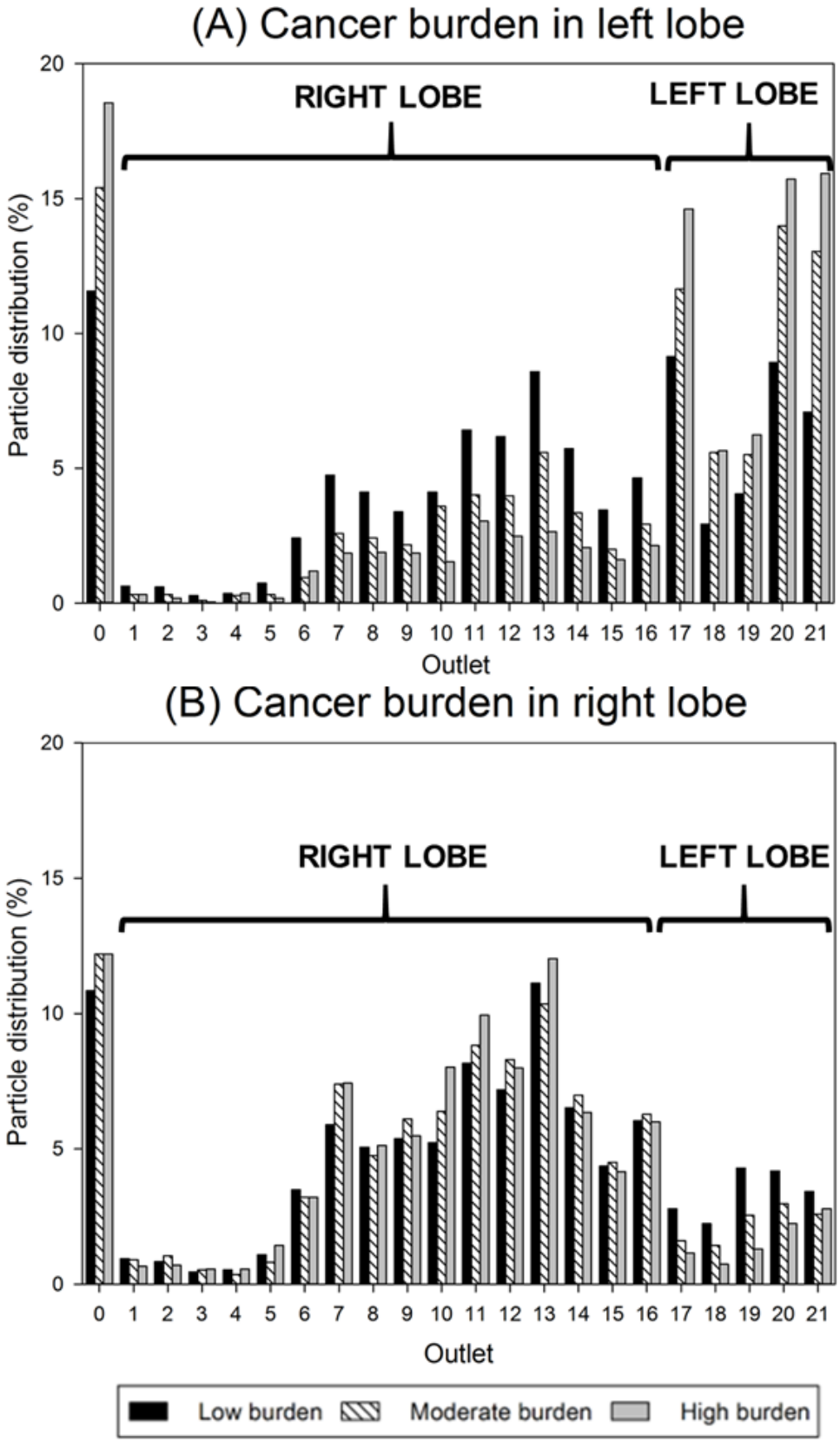
(A) Cancer burden in left lobe
RIGHT LOBE
LEFT LOBE
Particle distribution (%)
0
5
10
15
20
0 1 2 3 4 5 6 7 8 9 10 11 12 13 14 15 16 17 18 19 20 21
Outlet
(B) Cancer burden in right lobe
RIGHT LOBE
LEFT LOBE
Particle distribution (%)
0
5
10
15
20
0 1 2 3 4 5 6 7 8 9 10 11 12 13 14 15 16 17 18 19 20 21
Outlet
Low burden
Moderate burden
High burden